Title: Developmental Potassium Channel Maturation Enables Robust and Flexible Learning

Authors: Hiroyasu. Watanabe[1]*,

Affiliations:

[1] Bream Research Group; Kyoto, 603-8081, Japan.

*Corresponding author. Email: bream@dontokois.net

Abstract: Modern AI has flourished without molecular detail. Here I examine neural maturation in computational and molecular-physiological contexts. Immature transmission supports learning but collapses beyond task/load thresholds. A developmental screen identified KCNH7, upregulated in mouse cortex, incorporating its channel kinetics elevated spike threshold and stabilized recall, linking maturation to robustness without mechanistic elaboration. In unsupervised Restricted Boltzmann Machines, greater dynamical instability improved performance on complex tasks, highlighting a complementary regime. Developmentally plausible changes in KCNH7 conductance re-tuned reservoir dynamics and chaos, with appropriate levels improving memory and generalization, whereas excessive conductance degraded stability. Brief GPCR-like K^+ modulation balanced responsiveness and accuracy, suggesting neuromodulatory K^+ control as a lever for high-dimensional learning.

Main Text: Artificial intelligence now achieves human-level performance in perception, language, and navigation, yet its core architectures arose from neural theory (1) long before the molecular era—implying that rapid AI progress does not depend on detailed molecular knowledge.

By contrast, systems neuroscience has deeply characterized maturation: developmental shifts in synaptic and intrinsic properties that increase transmission speed and fidelity. The calyx of Held—a brainstem relay synapse for auditory timing—provides a canonical example (2), with well-documented maturation of presynaptic waveforms, EPSC kinetics, and plasticity (3–6). These principles likely generalize beyond audition, raising the question of how maturation supports robust computation in adult circuits.

Pseudo-immature transmission destabilizes learning despite initial acquisition in supervised and reinforcement models

I asked whether "immature" neural transmission degrades learning stability in conventional deep networks. Using a three-layer ReLU classifier on MNIST (784-50-50-10), I first confirmed that the control model rapidly acquired digit concepts and maintained high accuracy across extended trials (Fig. 1A). To mimic low-fidelity transmission, I added a uniform positive perturbation U[0.1, 1.0] to post-ReLU activations at every forward pass ("pseudo-immature transmission"). This manipulation did not prevent initial learning, but with continued training accuracy collapsed abruptly and the learned representation was lost (Fig. 1B). I then capped activations at 500, which did not avert the late-phase collapse (Fig. 1C).

Next, I varied optimization and regularization. With Adam, I used a lower learning rate (0.001) to keep control training stable, yet pseudo-immature transmission again produced late-phase failure (Fig. 1D,E). With dropout, I used a slightly higher learning rate (0.2) and the control remained stable, but adding pseudo-immature transmission still reproduced the collapse (Fig. 1F,G). Thus, forward-pass perturbations resembling immature transmission allow initial concept learning but reliably trigger catastrophic instability beyond a load/training threshold; common fixes (clipping, optimizer choice, dropout) did not prevent this failure mode.

I then tested a minimal reinforcement-learning setting (Q-learning in a 3×4 grid world with a single-layer function approximator). Under ReLU control, the agent learned a good policy (Fig. 2A). Adding a uniform U[0.65, 1.0] forward-pass perturbation caused divergence of action-value estimates and poor navigation (Fig. 2B). I applied gradient clipping (max-norm 5), which limited divergence but did not restore competent behavior when combined with pseudo-immature transmission (Fig. 2C,D). Forcing ReLU outputs >10 to zero produced instability even without added perturbations (Fig. 2E), whereas constant clipping at 10 avoided blow-ups (Fig. 2F). With a binary step activation, action-value divergence was not observed—even with perturbations—though expressivity was reduced (Fig. 2G,H). In sum, ReLU affords high expressivity yet is fragile to immature-like perturbations; binary responses are more robust but less flexible.

KCNH7 as a maturation-linked potassium channel that stabilizes spiking

I sought a molecular target that contributes to firing fidelity during development. As a working hypothesis, such genes should be expressed at higher levels in the adult brain than in the immature brain. Using the Allen Brain Atlas Data Portal, I screened potassium channels in the Developing Mouse Brain in situ hybridization dataset and shortlisted several candidates (Fig.

3A). Cross-referencing the adult P28 mouse cortex/hippocampus single-cell RNA-seq resource, I selected KCNH7 as a strong candidate (Fig. 3B).

The KCNH family (ERG/EAG/ELK) comprises voltage-gated, K^+-selective channels first described via Drosophila mutants sensitive to ether anesthesia (7). KCNH7 (Kv11.3) belongs to the ERG subfamily; its distinct gating yields large conductance on recovery from depolarization and can regulate resting potential and spike patterning in neurons (8–10). In the developmental in situ dataset, KCNH7 signals increase from ~P14 in forebrain, midbrain, and hindbrain regions, and Purkinje cells show higher expression at P56 compared with P28 (Fig. 3A). In single-cell data, KCNH7 is broadly expressed across excitatory and inhibitory types; in hippocampal populations its expression is negatively associated with Calb2 (calretinin; immature marker) and positively associated with Calb1 (calbindin; mature marker) (11,12) (Fig. 3C). These observations support a maturation-related role for KCNH7.

I next examined function by inserting KCNH7 kinetics into a conductance-based neuron model. Following prior work, I verified activation/deactivation time courses and found that my Hodgkin–Huxley-based formulation reproduces reported trends (Supplemental Table). In the baseline model, crossing threshold evokes sustained spiking during the current step (Fig. 4A). Increasing generic K-conductance raises rheobase but preserves this property (Fig. 4B). With KCNH7 inserted, the first-spike threshold increased and subsequent spikes were suppressed, stabilizing timing near threshold (Fig. 4C). A reported KCNH7 variant linked to bipolar spectrum disorder shifts $V_{½}$ by ~+10 mV and partially weakens this stabilization (13) (Fig. 4D). After symmetric Bernoulli thinning to 0.9× the minimum amp0 mean rate, KCNH7 showed the lowest CV_ISI, whereas the mutant partially reversed the effect; count-based discriminability (d′) was largest with increased fast K^+ conductance (High_K), indicating a timescale-dependent trade-off (Fig. 4E). Under high-frequency drive, the baseline model failed at 530 Hz, whereas High_K and KCNH7 preserved spiking; KCNH7 better sustained near-maximal responses at 300 Hz (Fig. 4F).

Effects of KCNH7-like properties in unsupervised learning models

I tested whether the KCNH7-like upward shift of spike threshold confers stability in an STDP spiking network (14). In the baseline configuration the network remained stable over prolonged training (Fig. 5A, control). Elevating spike thresholds (excitatory -42 mV, inhibitory -35 mV) slowed convergence relative to the low-threshold setting (-62 mV / -44 mV). To stress the system, I increased the learning rate (x70). With the nominal or low thresholds the proportion of "concordant" neurons periodically collapsed during continued learning, whereas the high-threshold network showed fewer and smaller collapses ($p < 0.05$ vs. low threshold at matched learning rate), consistent with increased robustness.

I next modulated randomness in a Restricted Boltzmann Machine (RBM) that generates MNIST digits. "Temperature" t scaled the logistic nonlinearity as sigma(x/t): $t = 1$ (standard), $t = 1/4$ (colder; more binary), and $t = 4$ (hotter; more linear). For single-class ("5") training, $t = 1$ yielded the best balance of speed and stability; $t = 1/4$ converged quickly, and $t = 4$ converged slowly with occasional divergence (Fig. 5B–D). For two-class ("5" and "1") training, outcomes flipped: with $t = 1/4$ the model often lost one class after initially learning both (21/150 runs ever reached >= 0.6 accuracy; 0/150 maintained >= 0.6 at 400,000 updates; Fig. 5F,H), whereas with $t = 4$ it more reliably retained both (57/150 reached >= 0.6; 49/150 maintained >= 0.6; Fig. 5G,I). At $t = 1$, 33/150 reached >= 0.6 and 14/150 maintained >= 0.6 (Fig. 5E). Together, these unsupervised results complement the spiking analysis: higher thresholds stabilize learned assemblies under perturbation, whereas a more linear response regime can favor retention of multiple concepts.

Direct Investigation into the Physiological Properties of Neural Maturation

I directly tested how KCNH7 influences network dynamics using a reservoir network constructed from a full-conductance Purkinje-cell model whose single-cell properties are characterized in Fig. 4. In the Mackey–Glass prediction task (Fig. 6A), introducing a physiological level of KCNH7 conductance improved prediction accuracy, whereas doubling the conductance degraded performance—likely because firing became overly suppressed. Consistently, the maximal Lyapunov exponent shifted from slightly positive (no KCNH7) to slightly negative (with KCNH7), indicating increased dynamical stability, and memory capacity peaked at the physiological conductance. Applying the same analyses to a KCNH7-mutant model (Fig. 4) shifted the conductance level that maximized performance upward, in parallel with corresponding shifts in the Lyapunov exponent and memory capacity. These findings support a conductance-dependent trade-off in which KCNH7 tunes stability versus representational power.

I next examined continuous learning trajectories for novel-concept acquisition by analyzing two transient phases across genotypes and conductance scales (Fig. 6B). In the unstable WT condition (scale = 2.0), the network adapted quickly at first but slower convergence followed because of divergent dynamics. In contrast, at the same scale the MUT network remained stably convergent, suggesting that a physiological switch—likely governed by input-dependent modulation—helps enforce proper stabilization.

mGluR1 (Gq-coupled) activation in Purkinje cells suppresses KCNH7 current, as shown by ERG blockade with E4031, and coincidentally shifts the KCNH7 $V_{1/2}$ by approximately +10 mV (10). I operationalized such GPCR-like modulation as brief “pulses” that raise the activation shift (vshift) from 0 mV (WT baseline) to +10 mV (MUT-like) during predefined windows, while otherwise maintaining the WT setting. Across 30 random seeds, the GPCR-pulse schedule reduced mean Phase-A test MSE by 55.4% relative to WT (0.1561 ± 0.0002 vs. 0.3502 ± 0.0001), although MUT-only remained best (0.1387 ± 0.0006; +12.5% lower than GPCR-pulse). In Phase-B, GPCR-pulse and MUT-only were virtually identical (0.0849 ± 0.0000 vs. 0.0848 ± 0.0000; $\Delta = 0.0001$, +0.12%), both far better than WT (≈ −75% vs. WT). Early in training, cumulative-MSE endpoints favored GPCR-pulse over both WT and MUT (Welch’s t, all $p < 10^{-6}$), indicating faster convergence. Together, transient vshift pulses delivered MUT-level final accuracy without permanently locking the network into the MUT state, suggesting a neuromodulatory “burst-gating” mechanism that speeds learning while preserving stability between pulses.

Finally, to relate maturation to cortical information processing, I analyzed in vivo two-photon Visual Behavior recordings (https://portal.brain-map.org/circuits-behavior/visual-behavior-2p) from mice aged P95–223 (Fig. 6D). The participation ratio (PR) declined with age ($r = -0.30$, $p < 0.01$), whereas the activation time constant (τ) and behavioral sensitivity index d' were stable. PR correlated positively with d' ($r = 0.21$, $p < 0.05$) but not with τ. Robust regression showed a modest positive effect of PR on d' ($\beta = 0.12$, $p = 0.014$), explaining < 4% of the variance and dominated by between-mouse variability (ICC ≈ 0.48). These results suggest that late-stage maturation reduces representational dimensionality via network-level refinement rather than intrinsic firing changes, and that maintaining higher dimensionality can support stronger behavioral performance.

Conclusions

Both the supervised and reinforcement-learning models showed that prolonged training under random (pseudo-immature) transmission led to loss of the learned representation (Figs. 1, 2). In practice this failure arose from divergent activations. Even when I imposed output clipping—as a proxy for biophysical saturation—similar collapses occurred (Fig. 1C). Likewise, gradient clipping curbed explosive updates but did not prevent degradation of action learning (Fig. 2D). Comparisons in Fig. 2E–F suggest that outright failures to spike (or to propagate a usable signal) impair learning more severely than merely reaching a high maximal response rate. Notably, introducing KCNH7 properties alleviated these limitations and preserved performance under high-rate drive (Fig. 4F).

These instabilities are superficially reminiscent of catastrophic forgetting (15), which is typically studied across task switches. Here, however, the collapse followed continuous training on a fixed task with injected randomness, implying that variability in the transmission pathway can mimic dataset perturbations. Crucially, the failures appeared under ReLU but not under the binary step function (Fig. 2G), and comparable sensitivities to "temperature" (randomness) were reproduced in the Restricted Boltzmann Machine (RBM) setting (Fig. 5B, 5C). Under high temperature (high randomness), representations eroded over extended training.

When task complexity increased (learning a pair of digits with the RBM), the pattern inverted: low temperature yielded rapid initial convergence but then destabilized, whereas higher temperature supported continued improvement and stable two-concept recall (Fig. 5E–G). Thus, the optimal operating point depends on representational demands: robust, low-frequency stability for simple mappings, versus controlled variability for higher-dimensional structure.

These observations align with the expression pattern and physiology of KCNH7. KCNH7 is more abundant in mature neurons (Fig. 3A), and its kinetics raise spike threshold while linearizing the input–output relation (Fig. 4C). In my simulations, KCNH7 reduced spike-train irregularity after fair, model-agnostic rate matching (Fig. 4E) and stabilized recall in unsupervised settings (Fig. 5A). In short, higher threshold supports stability, and a more linear response supports reliable credit assignment; together they provide a simple mechanistic account of maturation-linked robustness. At the same time, Fig. 5 indicates that some degree of dynamical richness is beneficial for complex inference—suggesting that maturation balances stability with flexibility rather than maximizing either alone.

A plausible biological lever for this balance is neuromodulation. Chronic fluoxetine can "demature" adult granule cells via 5-HT4 receptors (16), a Gs-coupled receptor known to activate PKA (17) and reported to engage PKCα in intestinal epithelium (18). In Purkinje cells, mGluR1 activation suppresses ERG/K^+ current (KCNH family) and shifts V1/2 by ¥~+10 mV (10). Consistent with the KANPHOS database (https://kanphos.jp/), KCNH7 is phosphorylated by PKC, providing a route for GPCR control. In silico, brief "GPCR-like" pulses that transiently shifted the KCNH7 activation curve accelerated learning to near MUT-level accuracy while preserving stable dynamics between pulses (Fig. 6C). This supports a "burst-gating" view in which well-timed neuromodulatory bouts move the circuit to a high-plasticity regime and then release it back to a stable baseline. Conversely, tonic or mistimed modulation could degrade function, offering a mechanistic link to maladaptive plasticity.

These results motivate targeted experiments: (i) test whether mGluR1 produces a rapid, PKC-dependent positive shift in KCNH7 V1/2 in Purkinje cells; (ii) quantify the kinetics and amplitude of this shift during patterned input in slices; and (iii) compare closed-loop, state-dependent delivery of neuromodulatory pulses with tonic stimulation in behavioral learning paradigms. Such timing-aware strategies may capture the benefits of enhanced excitability and plasticity without the liabilities of persistent ERG suppression.

Several limitations temper the conclusions. Owing to data availability, my in vivo analyses sampled a late-maturation window (postnatal day ≥ 95). Within this range I did not observe systematic changes in intrinsic firing proxies, yet participation ratio declined with age and related positively to behavioral d′ (Fig. 6D), suggesting network-level refinement rather than intrinsic re-tuning. Additional work is needed to link KCNH7 conductance changes to population dynamics in vivo and to establish causal roles in disorders such as bipolar spectrum disorder, where KCNH7 variation has been implicated.

Artificial intelligence is, by design, “artificial,” yet it already approximates many human cognitive functions. This proximity allows computational models to illuminate how molecular mechanisms—such as maturation of ion-channel kinetics—shape learnability and stability. While the present study is intentionally simple, its convergence across supervised, reinforcement, unsupervised, and reservoir settings argues that KCNH7-like maturation provides a general pathway to robust computation, and that neuromodulatory K^+ control may be a key lever for flexibly trading off stability and plasticity in the adult brain. Taken together, these results argue that bridging algorithmic simulations with precise molecular manipulations is essential; I expect this union to catalyze the field’s next breakthroughs.

References and Notes

1. Amari S. Backpropagation and stochastic gradient descent method. *Neurocomputing* **5**, 185-196 (1993).

2. Takahashi T. Strength and precision of neurotransmission at mammalian presynaptic terminals. *Proceedings of the Japan Academy Series B* **91**, 305-320 (2015).

3. Koike-Tani M, Saitoh N, Takahashi T. Mechanisms Underlying Developmental Speeding in AMPA-EPSC Decay Time at the Calyx of Held. *J Neurosci.* **25**, 199-207 (2005).

4. Taschenberger H and von Gersdorff H. Fine-Tuning an Auditory Synapse for Speed and Fidelity: Developmental Changes in Presynaptic Waveform, EPSC Kinetics, and Synaptic Plasticity. *J neurosci.* **20**, 9162-9173 (2000).

5. Yamashita T, Eguchi K, Saitoh N, von Gersdorff H, Takahashi T. Developmental shift to a mechanism of synaptic vesicle endocytosis requiring nanodomain Ca2+. *Nat Neurosci.* **13**, 838–844 (2010).

6. Yang YM and Wang LY. Amplitude and Kinetics of Action Potential-Evoked Ca2+ Current and Its Efficacy in Triggering Transmitter Release at the Developing Calyx of Held Synapse. *J Neurosci.* **26**, 5698–5708 (2006).

7. Brüggemann A, Pardo LA, Stühmer W, Pongs O. Ether-à-go-go encodes a voltage-gated channel permeable to K+ and Ca2+ and modulated by cAMP. *Nature* **365**, 445-448 (1993).

8. Perry M, Sanguinetti M, Mitcheson J. Revealing the structural basis of action of hERG potassium channel activators and blockers. *J Physiol.* **588**, 3157-3167 (2010).

9. Akbarali HI, Thatte H, He XD, Giles WR, Goyal RK. Role of HERG-like K(+) currents in opossum esophageal circular smooth muscle. *Am J Physiol.* **277**, C1284-1290 (1999).

10. Niculescu D, Hirdes W, Hornig W, Pongs O, Schwarz JR. Erg Potassium Currents of Neonatal Mouse Purkinje Cells Exhibit Fast Gating Kinetics and Are Inhibited by mGluR1 Activation. *J Neurosci.* **33**, 16729-16740 (2013).

11. Iacopino AM, Rhoten WB, Christakos S. Calcium binding protein (calbindin-D28k) gene expression in the developing and aging mouse cerebellum. *Brain Res Mol Brain Res.* 8, 283-290 (1990).

12. Brandt MD, Jessberger S, Steiner B, Kronenberg G, Reuter K, Bick-Sander A, von der Behrens W, Kempermann G. Transient calretinin expression defines early postmitotic step of neuronal differentiation in adult hippocampal neurogenesis of mice. *Mol Cell Neurosci.* **24**, 603-613 (2003).

13. Strauss KA, Markx S, Georgi B, Paul SM, Jinks RN, Hoshi T, McDonald A, First MB, Liu W, Benkert AR, Heaps AD, Tian Y, Chakravarti A, Bucan M, Puffenberger EG. A population-based study of KCNH7 p.Arg.394His and bipolar spectrum disorder. *Mol Genet.* **23**, 6395-6406 (2014).

14. Diehl PU, Cook M. Unsupervised learning of digit recognition using spike-timing-dependent plasticity. *Front Comput Neurosci.*, 9:99 (2015).

15. Kirkpatricka J, Pascanua R, Rabinowitza N, Venessa J, Desjardinsa G, Rusua AA, Milana K, Quana J, Ramalhoa T, Grabska-Barwinskaa A, Hassabisa D, Clopathb C, Kumarana D, Hadsella R. Overcoming catastrophic forgetting in neural networks. *Proc Natl Acad Sci USA*. **114**, 3521-3526 (2017).

16. Kobayashi K, Ikeda Y, Sakai A, Yamasaki N, Haneda E, Miyakawa T, Suzuki H. Reversal of hippocampal neuronal maturation by serotonergic antidepressants. *Proc Natl Acad Sci USA.* **107**, 8434-8439 (2010).

17. Torres GE, Arfken CL, Andrade R. 5-Hydroxytryptamine4 receptors reduce afterhyperpolarization in hippocampus by inhibiting calcium-induced calcium release5-Hydroxytryptamine4 receptors reduce afterhyperpolarization in hippocampus by inhibiting calcium-induced calcium release. *Mol Pharmacol.* **50**, 1316-1322 (1996).

18. Gill RK, Saksena S, Tyagi S, Alrefai WA, Malakooti J, Sarwar Z, Turner JR, Ramaswamy K, Dudeja PK. Serotonin inhibits Na+/H+ exchange activity via 5-HT4 receptors and activation of PKCα in human intestinal epithelial cells. *Gastroenterology* **128**, 962-974 (2005).

19. Tsuboi D, Otsuka T, Shimomura T, Faruk MO, Yamahashi Y, Amano M, Funahashi Y, Kuroda K, Nishioka T, Kobayashi K, Sano H, Nagai T, Yamada K, Tzingounis AV, Nambu A, Kubo Y, Kawaguchi Y, Kaibuchi K. Dopamine drives neuronal excitability via KCNQ channel phosphorylation for reward behavior. *Cell Rep.*, **40**, 111309 (2022).

20. Kozareva V, Martin C, Osorno T, Rudolph S, Guo C, Vanderburg, Nadaf N, Regev A, Regehr WG, Macosko E. A transcriptomic atlas of mouse cerebellar cortex comprehensively defines cell types. *Nature* **598**, 214-219 (2021).

Acknowledgments:

I am thankful for the kind support of Junichiro Yoshimoto for discussions and comments on my work. Hiroshi Watanabe, Yukihiro Nakamura and Atsuhito Toyomaki also provided comments and support for my work.

Competing interests:

The author declares no competing interests.

Data and Code Deposition:

All analytical code in the main text and Supplementary Materials is available in the GitHub repository at https://github.com/BreamResearch/Neural-Maturation, which will be made public upon acceptance of this article.

Fig. 1.

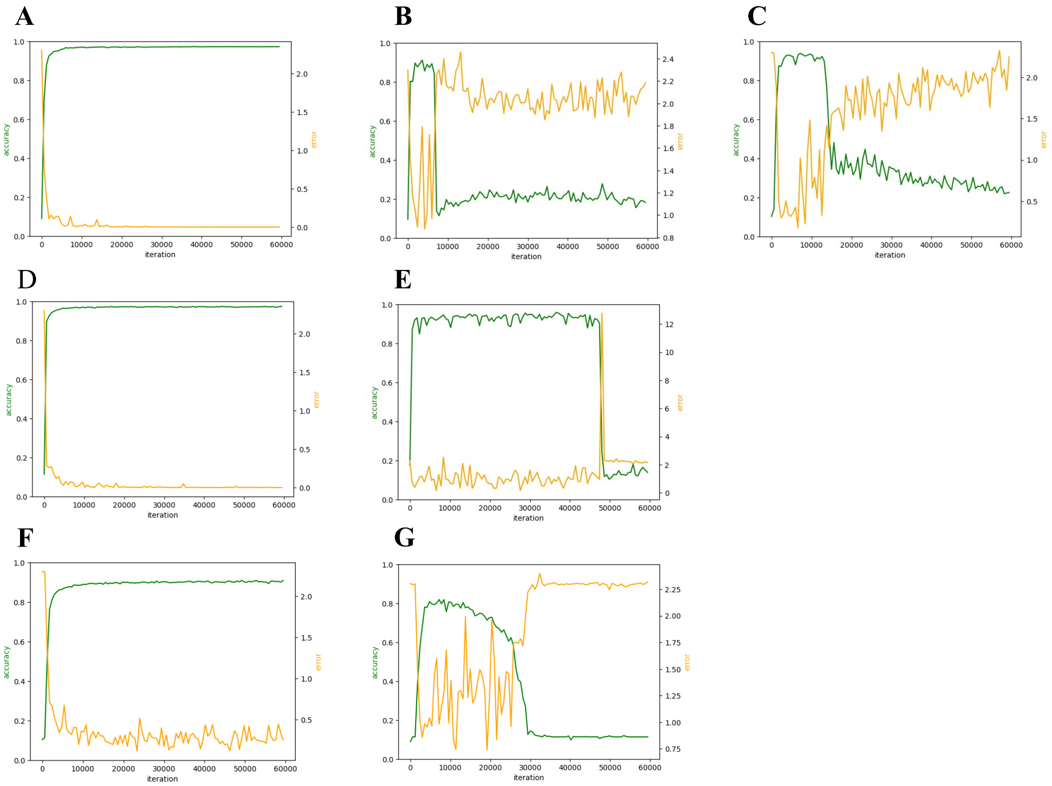
A
B
C
D
E
F
G
accuracy
error
iteration
0.0
0.2
0.4
0.6
0.8
1.0
0
10000
20000
30000
40000
50000
60000
0.0
0.5
1.0
1.5
2.0
0.8
1.0
1.2
1.4
1.6
1.8
2.0
2.2
2.4
0
2
4
6
8
10
12
0.75
1.00
1.25
1.50
1.75
2.00
2.25

Fig. 1. Pseudo-immature transmission destabilizes supervised MNIST learning.

MNIST classification with a fully connected 784–50–50–10 network (ReLU). "Pseudo-immature" transmission was implemented as additive forward-pass noise r is sampled uniformly from [0.1, 1.0] to ReLU activations. ReLU outputs were capped at 500 in the clipping condition. Accuracy (green, left axis) and loss (orange, right axis) are plotted over training iterations. (A) Baseline (learning rate 0.1). (B) Additive noise (pseudo-immature). (C) Additive noise with ReLU output clipping at 500. (D) Adam optimizer, baseline. (E) Adam optimizer with additive noise (learning rate 0.001). (F) Dropout, baseline. (G) Dropout with additive noise (learning rate 0.2). See code repository for architecture and training hyperparameters.

Fig. 2.

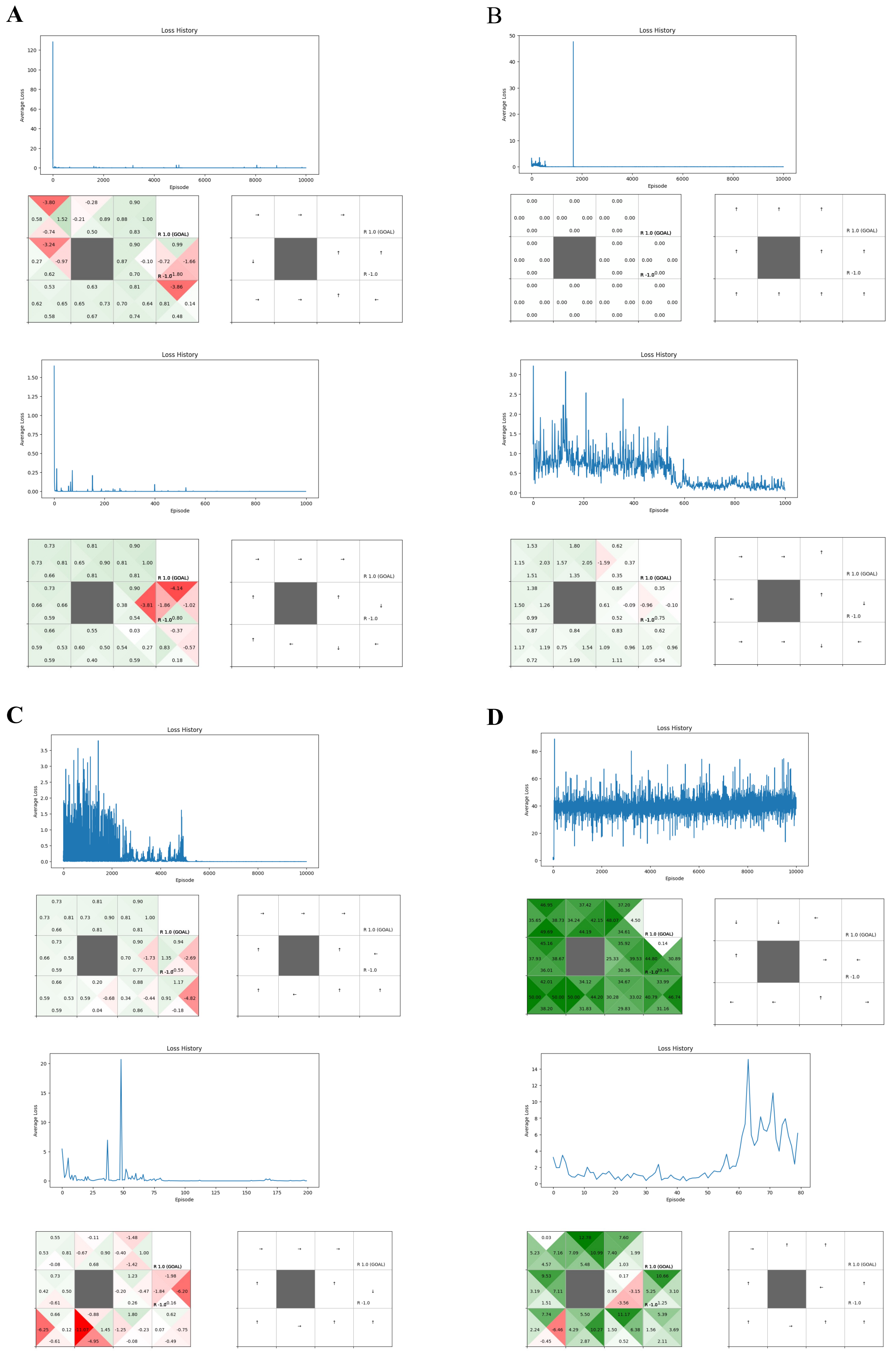
A
B
C
D
Loss History
Average Loss
Episode
0
2000
4000
6000
8000
10000
200
400
600
800
1000
25
50
75
100
125
150
175
R 1.0 (GOAL)
R -1.0
→
↑
↓
←

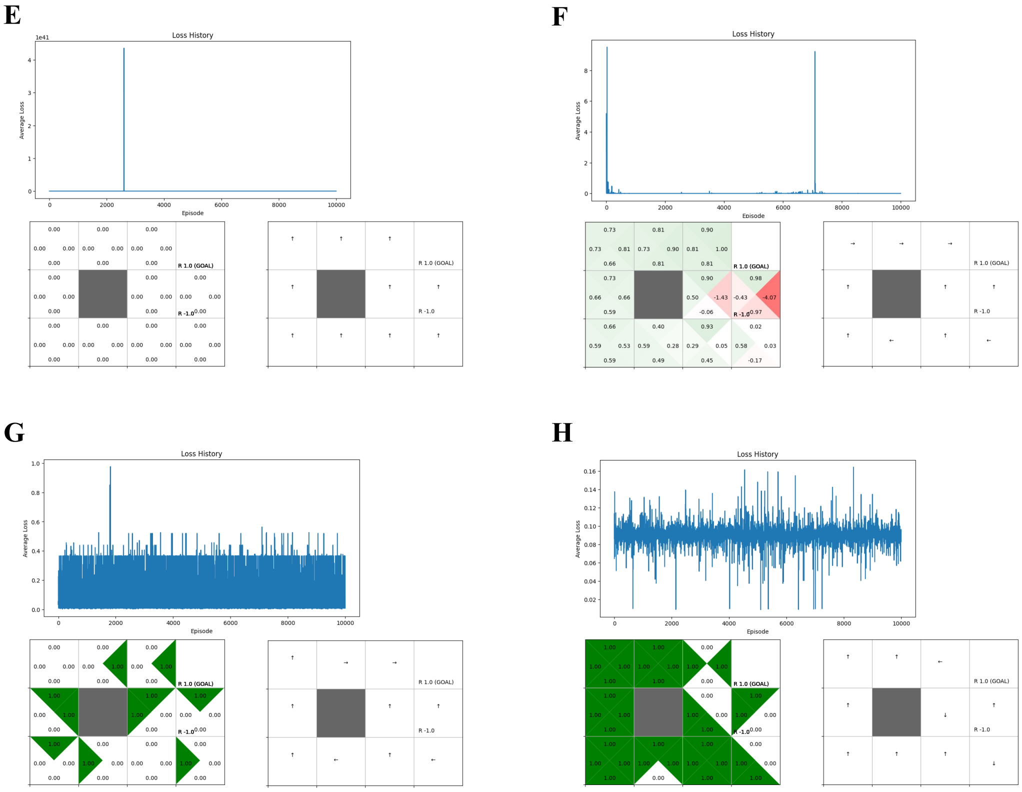
E
Loss History
1e41
Average Loss
Episode
R 1.0 (GOAL)
R -1.0
F
Loss History
Average Loss
Episode
0.73
0.81
0.90
0.66
0.50
-1.43
-0.43
-4.07
0.98
-0.06
-0.97
0.93
0.02
0.59
0.53
0.28
0.29
0.05
0.58
0.03
0.49
0.45
-0.17
R 1.0 (GOAL)
R -1.0
G
Loss History
Average Loss
Episode
R 1.0 (GOAL)
R -1.0
H
Loss History
Average Loss
Episode
R 1.0 (GOAL)
R -1.0

Fig. 2. Effects of pseudo-immature transmission in a Q-learning grid-world.

A 3×4 maze task was solved with tabular Q-learning implemented by a single-layer network (implementation adapted from the “grid world” in the cited repository). The agent starts each episode at the bottom-left cell, selects actions from the learned state–action values, remains in place without penalty when attempting to move into a wall, and upon reaching the goal receives reward and resets to the start for the next episode. During “pseudo-immature” transmission, a uniform random value was injected into the forward pass: `r ~ Uniform(0.65, 1.0)`. Additional manipulations included ReLU output clipping at 50, gradient clipping at 5, and a binary Step activation that maps outputs >0.5 to 1 and ≤0.5 to 0. The main plots show loss versus episode; insets depict the learned action values at each grid cell and the corresponding preferred next-step directions. Panel conditions: (A) ReLU (baseline). (B) ReLU with random forward transmission. (C) ReLU with gradient clipping (max 5). (D) ReLU with gradient clipping (max 5) plus random transmission. (E) ReLU with hard zeroing of activations exceeding 10. (F) ReLU with output clipped at 10. (G) Step activation. (H) Step activation with random forward transmission.

Fig. 3.

A

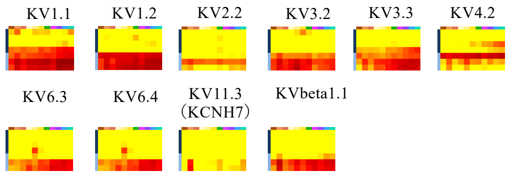

URL:https://developingmouse.brain-map.org/gene/show/82041

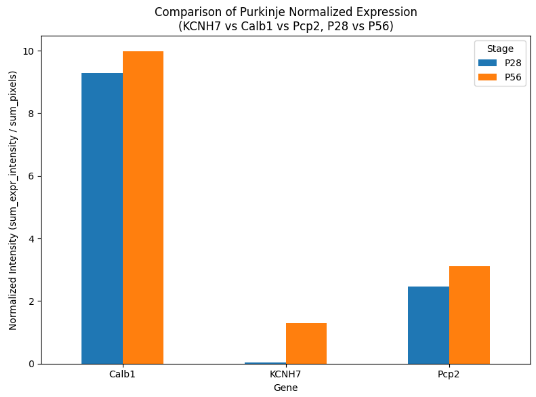

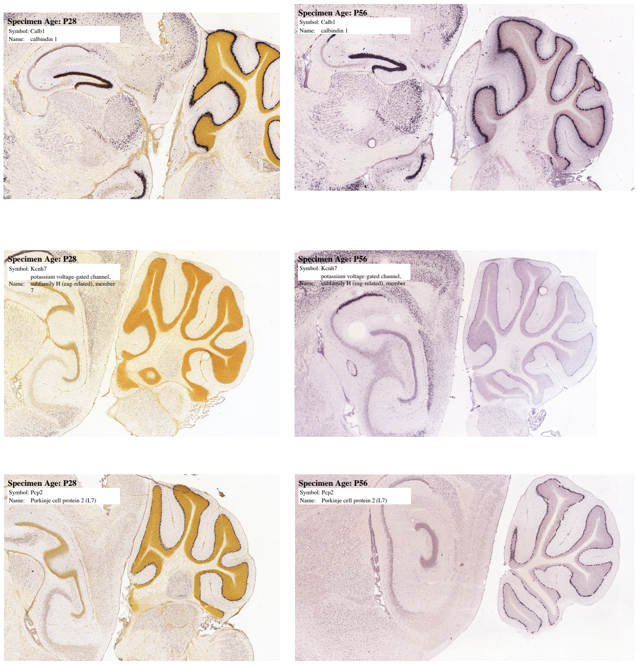
Specimen Age: P28
Symbol: Calb1
Name: calbindin 1
Specimen Age: P56
Symbol: Calb1
Name: calbindin 1
Specimen Age: P28
Symbol: Kcnh7
Name: potassium voltage-gated channel, subfamily H (eag-related), member 7
Specimen Age: P56
Symbol: Kcnh7
Name: potassium voltage-gated channel, subfamily H (eag-related), member 7
Specimen Age: P28
Symbol: Pcp2
Name: Purkinje cell protein 2 (L7)
Specimen Age: P56
Symbol: Pcp2
Name: Purkinje cell protein 2 (L7)

B

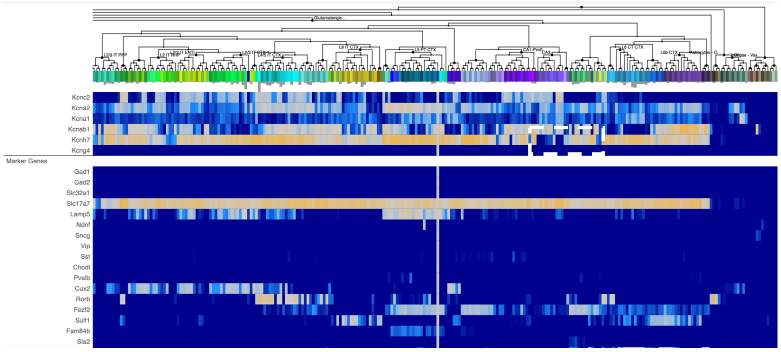

C

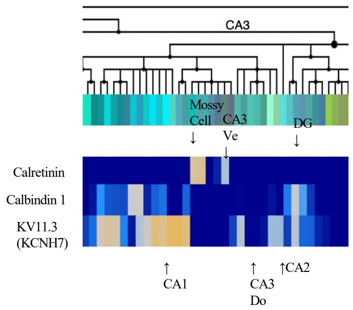

URL:https://celltypes.brain-map.org/rnaseq/mouse_ctx-hpf_10x?selectedVisualization=Heatmap&colorByFeature=Cell+Type&colorByFeatureValue=Gad1

Fig. 3. Candidate potassium channels with higher expression in the mature mouse brain.

(A) Developmental in situ hybridization (ISH) summaries from the Allen Developing Mouse Brain Atlas (URL shown in panel). Small heatmaps display gene expression with developmental stages on the vertical axis (E11.5, E13.5, E15.5, E18.5, P4, P14, P28) and brain regions on the horizontal axis (Allen acronyms: RSP, Tel, PedHy, p3, p2, p1, M, PPH, PH, PMH, MH). Color scale indicates expression intensity (low to high). Right: ISH images for KCNH7 in mouse cerebellum at P28 and P56; signal is localized to the Purkinje cell layer (20). Bar plot: normalized Purkinje-cell expression at P28 and P56 for Calb1, KCNH7, and Pcp2. Quantification: for each experiment (P28/P56; experiment IDs listed in code), Structure Unionize records whose structure name contained “Purkinje” were retrieved, values were summed across Purkinje subregions, and normalized intensity was computed as (Σ sum_expressing_pixel_intensity) / (Σ sum_pixels). (B) Single-cell RNA-seq heatmap from the Allen Cell Types database (P28 mouse cortex–hippocampus dataset; URL shown). Columns denote cell-type clusters; rows denote genes; color denotes normalized expression. (C) Enlarged view of hippocampal clusters highlighted in (B). Rows show Calretinin (Calb2), Calbindin1 (Calb1), and KCNH7; columns correspond to hippocampal cell-type groups (e.g., CA fields and dentate gyrus). Color denotes normalized expression.

Fig 4.

A Purkinje model original: 8.11pA(300-800ms)

Purkinje model original: 8.12pA(300-800ms)

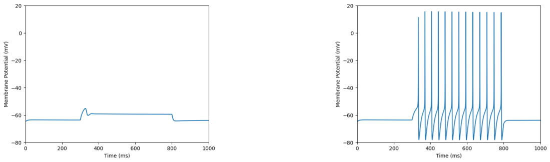

B High K conductance: 15.81pA(300-800ms)

High K conductance: 15.82pA(300-800ms)

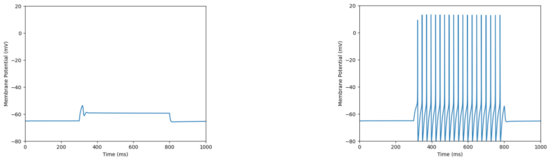

D KCNH7: 13.2pA

KCNH7_mut: 11.2pA

+0.05pA

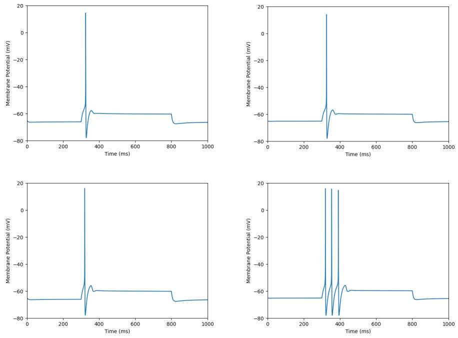

D +KCNH7: 13.2pA(300-800ms)

+KCNH7: 15pA(300-800ms)

+KCNH7: 15.4pA(300-800ms)

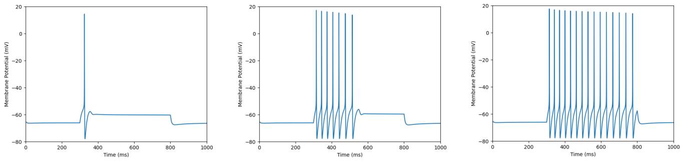

E

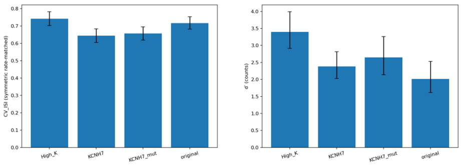

F

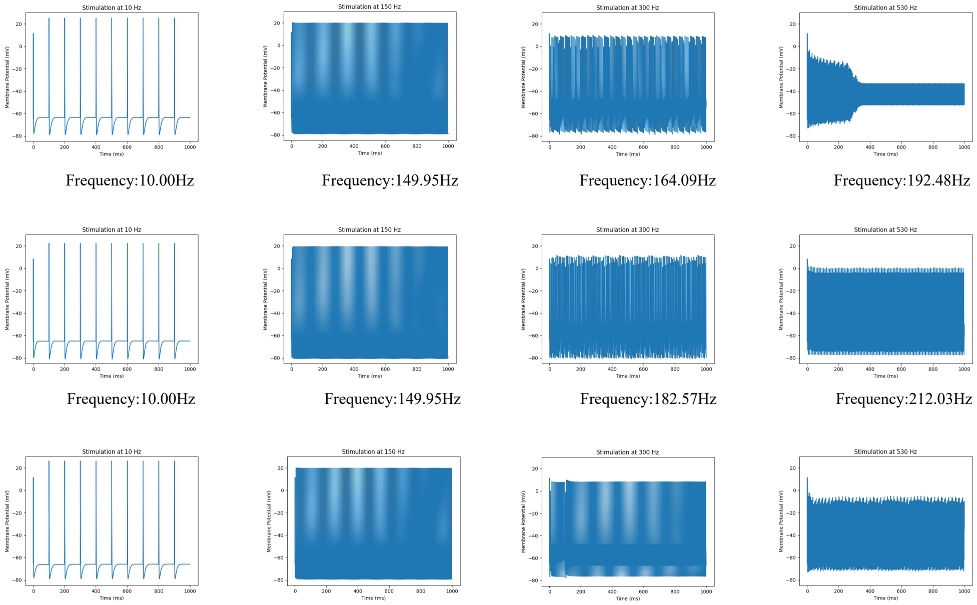

Original

Frequency:10.00Hz Frequency:149.95Hz Frequency:164.09Hz Frequency:192.48Hz

High_K

Frequency:10.00Hz Frequency:149.95Hz Frequency:182.57Hz Frequency:212.03Hz

KCNH7

Frequency:10.00Hz Frequency:149.95Hz Frequency:150.99Hz Frequency:198.31Hz

Fig. 4. Functions of KCNH7 for neural fidelity and linear responses.

Examine the effects of KCNH7 parameter insertion in Purkinje cell model. The KCNH7 neuron was simulated using the NEURON simulator (https://www.neuron.yale.edu/neuron/). The basic Purkinje model and KCNH7 parameters were taken from Niculescu et al.. The KCNH7 kinetics parameters were estimated based on the protocol described in their work (10). (A) Baseline Purkinje-cell model: threshold crossing (300–800 ms step) evokes sustained spiking. (B) Increasing generic K-conductance raises rheobase. (C) Inserting KCNH7 kinetics raises first-spike threshold and suppresses subsequent spikes, stabilizing timing near threshold. (D) Pseudo-mutant with +10 mV V½ partially loses stabilization (13). (E) Rate-matched spike-train irregularity and discriminability. Bars show mean CV_ISI (left) from 1-s spike trains after Bernoulli thinning to 0.9× the minimum amp0 mean rate across models, and mean d′ (right) from spike counts (amp1 vs amp0), computed as $d' = (\mu\_a1 - \mu\_a0)/\sqrt{((\sigma\_a0^2+\sigma\_a1^2)/2)}$. Error bars: 95% bootstrap CIs across seeds ($n = 50$). Spikes were detected at −20 mV in NEURON simulations; input noise combined Poisson ($\lambda = 0.005$ per step) and Gaussian ($\sigma = 0.1$ nA). DC baselines were near rheobase per model; $\Delta I = +20\%$ of baseline. (F) High-frequency drive (10, 150, 300, 530 Hz): baseline failed at 530 Hz; High_K and KCNH7 maintained spiking, with KCNH7 better sustaining near-maximal responses at 300 Hz.

Fig. 5.

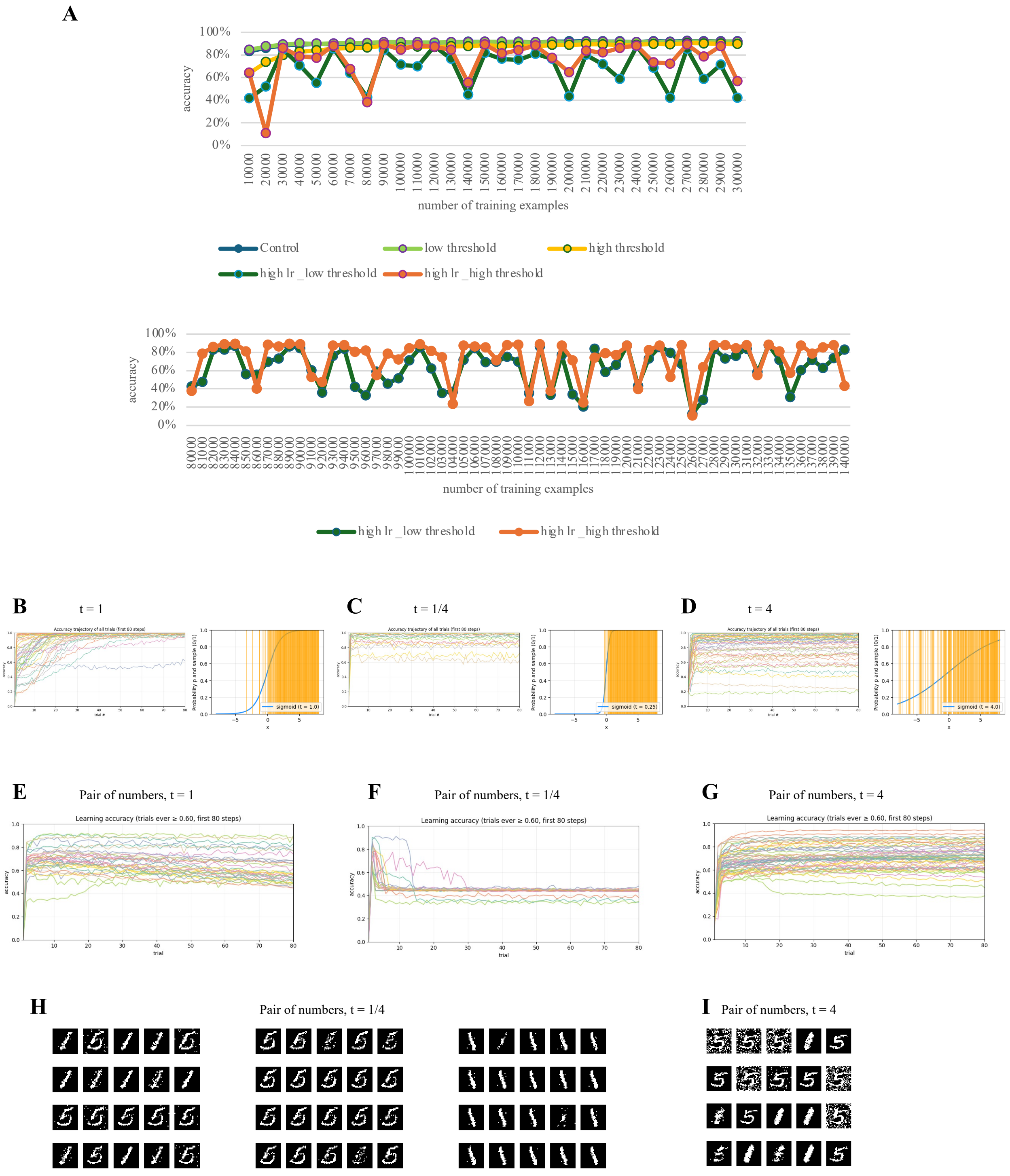
A
100%
80%
60%
40%
20%
0%
accuracy
10000
20000
30000
40000
50000
60000
70000
80000
90000
100000
110000
120000
130000
140000
150000
160000
170000
180000
190000
200000
210000
220000
230000
240000
250000
260000
270000
280000
290000
300000
number of training examples
Control
low threshold
high threshold
high lr _low threshold
high lr _high threshold
100%
80%
60%
40%
20%
0%
accuracy
number of training examples
high lr _low threshold
high lr _high threshold
B
t = 1
Accuracy trajectory of all trials (first 80 steps)
accuracy
trial #
Probability p and sample (0/1)
sigmoid (t = 1.0)
x
C
t = 1/4
Accuracy trajectory of all trials (first 80 steps)
sigmoid (t = 0.25)
D
t = 4
Accuracy trajectory of all trials (first 80 steps)
sigmoid (t = 4.0)
E
Pair of numbers, t = 1
Learning accuracy (trials ever ≥ 0.60, first 80 steps)
accuracy
trial
F
Pair of numbers, t = 1/4
Learning accuracy (trials ever ≥ 0.60, first 80 steps)
G
Pair of numbers, t = 4
Learning accuracy (trials ever ≥ 0.60, first 80 steps)
H
Pair of numbers, t = 1/4
I
Pair of numbers, t = 4

Figure 5. Effects of KCNH7-like properties in unsupervised learning models

(A) STDP spiking network (14). Learning rate (Lr) and spike thresholds were varied for excitatory (E) and inhibitory (I) neurons. Low-threshold: E = -62 mV, I = -44 mV. High-threshold: E = -42 mV, I = -35 mV. Top: default Lr; bottom: Lr x 70. Y-axis: proportion of “concordant” neurons between training and test. X-axis: number of training examples (evaluated every 1,000 trials). (B–D) RBM single-digit (“5”) experiments. Architecture: 784–256 RBM trained with Contrastive Divergence on 5,000 training images per cycle; 80 evaluation cycles (total 400,000 parameter updates). Accuracy was scored by a fixed supervised classifier (Fig. 1) on all test digits for the target class. Temperature t scales the logistic nonlinearity sigma(x/t): t = 1 (B), t = 1/4 (C), t = 4 (D). Left panels: accuracy trajectories across trials. Right insets: sigma(x/t) (blue) and sampling probabilities (orange) versus input x. Y-axis: accuracy. X-axis: trial number (each trial adds 5,000 updates). (E–G) RBM two-digit (“5” and “1”) experiments under the same protocol as (B–D). Accuracy per trial over 80 evaluation cycles for t = 1 (E), t = 1/4 (F), and t = 4 (G). (H–I) Representative generated samples from runs in (F) and (G), respectively. Each panel shows multiple draws at the end of training for the two-digit setting.

Fig. 6.

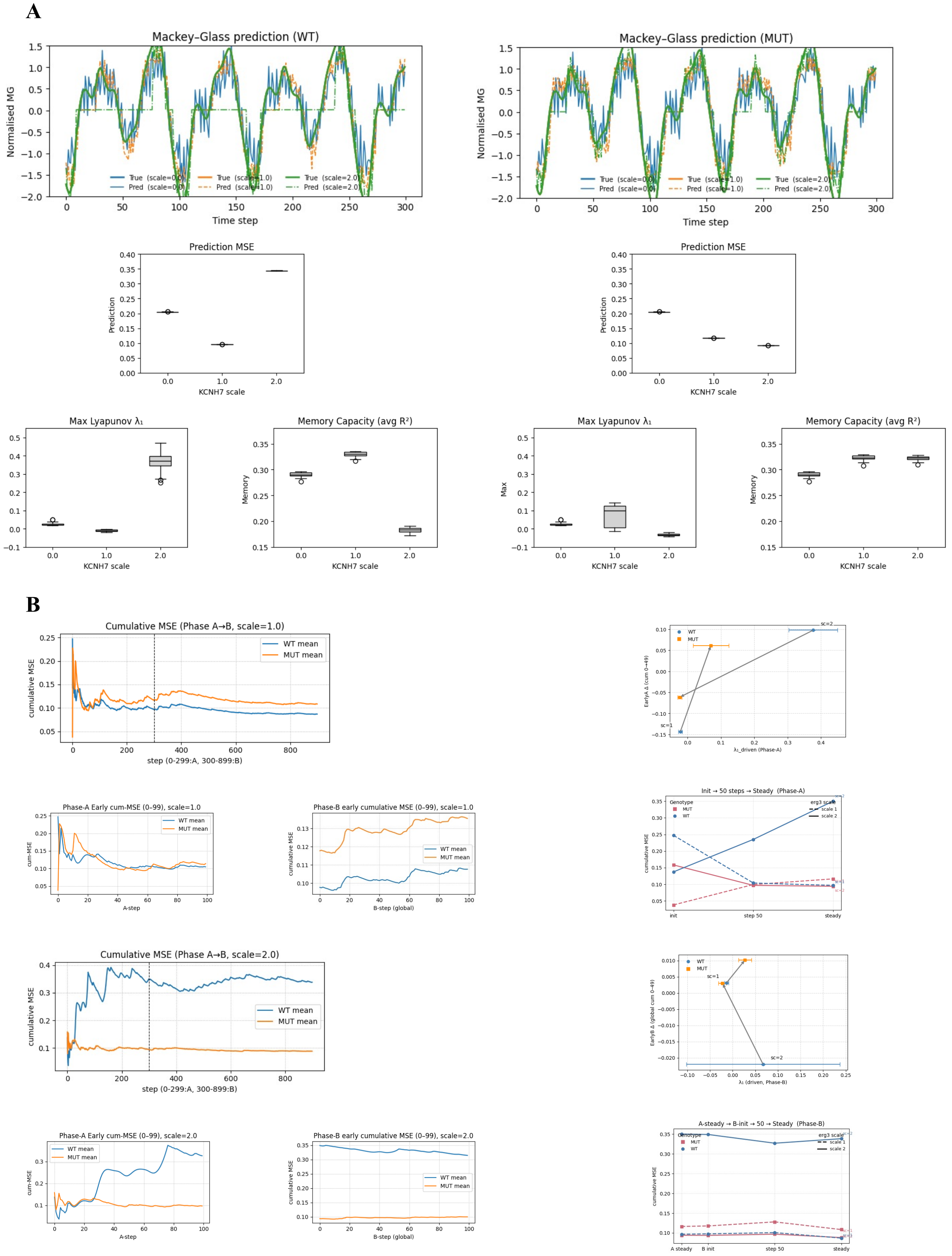
A
Mackey–Glass prediction (WT)
Normalised MG
Time step
True (scale=0.0)
Pred (scale=0.0)
True (scale=1.0)
Pred (scale=1.0)
True (scale=2.0)
Pred (scale=2.0)
Mackey–Glass prediction (MUT)
Normalised MG
Time step
Prediction MSE
Prediction
KCNH7 scale
Prediction MSE
Prediction
KCNH7 scale
Max Lyapunov λ₁
Max
KCNH7 scale
Memory Capacity (avg R²)
Memory
KCNH7 scale
Max Lyapunov λ₁
Max
KCNH7 scale
Memory Capacity (avg R²)
Memory
KCNH7 scale
B
Cumulative MSE (Phase A→B, scale=1.0)
cumulative MSE
step (0-299:A, 300-899:B)
WT mean
MUT mean
WT
MUT
sc=2
sc=1
EarlyA Δ (cum 0→49)
λ₁_driven (Phase-A)
Phase-A Early cum-MSE (0–99), scale=1.0
cum-MSE
A-step
WT mean
MUT mean
Phase-B early cumulative MSE (0–99), scale=1.0
cumulative MSE
B-step (global)
WT mean
MUT mean
Init → 50 steps → Steady (Phase-A)
cumulative MSE
Genotype
MUT
WT
erg3 scale
scale 1
scale 2
init
step 50
steady
sc=1
sc=2
Cumulative MSE (Phase A→B, scale=2.0)
cumulative MSE
step (0-299:A, 300-899:B)
WT mean
MUT mean
WT
MUT
sc=1
sc=2
EarlyB Δ (global cum 0–49)
λ₁ (driven, Phase-B)
Phase-A Early cum-MSE (0–99), scale=2.0
cum-MSE
A-step
WT mean
MUT mean
Phase-B early cumulative MSE (0–99), scale=2.0
cumulative MSE
B-step (global)
WT mean
MUT mean
A-steady → B-init → 50 → Steady (Phase-B)
cumulative MSE
Genotype
MUT
WT
erg3 scale
scale 1
scale 2
A steady
B init
step 50
steady
sc=1
sc=2

C

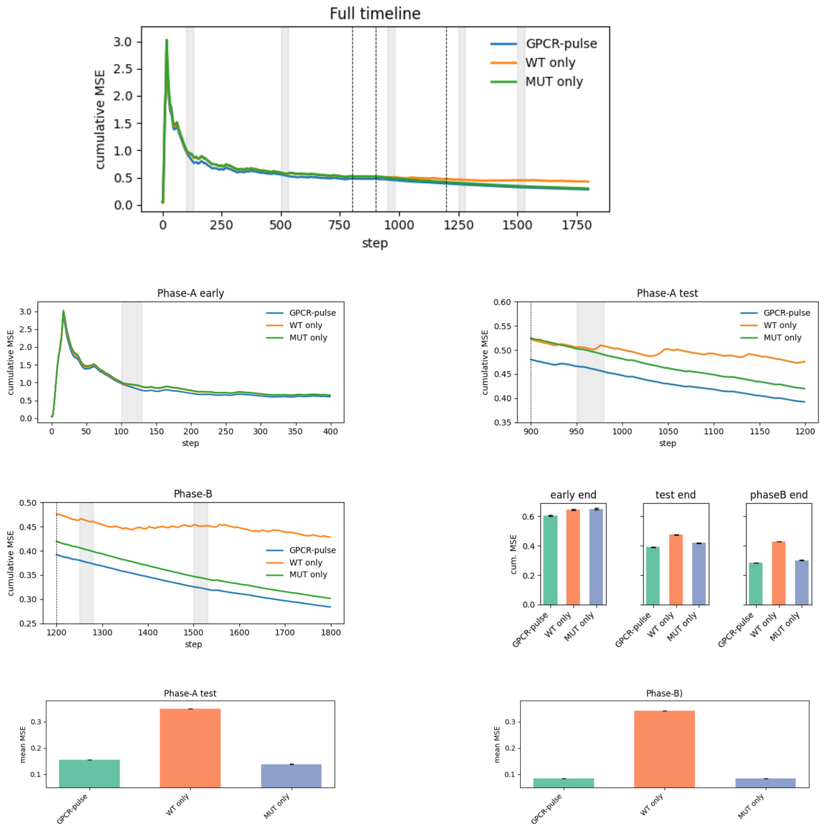

D

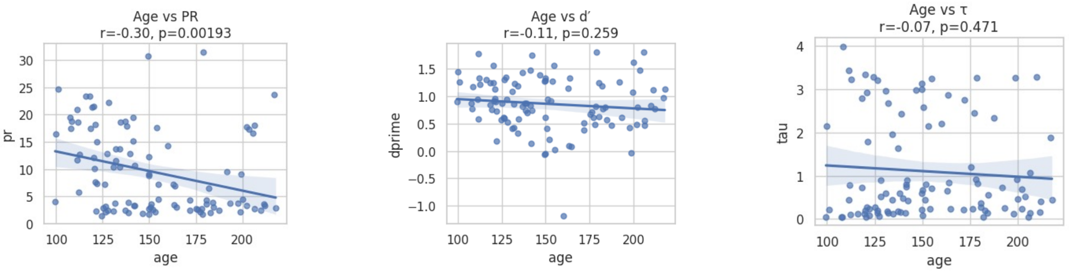

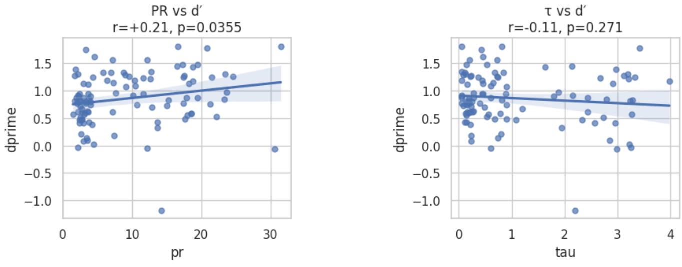

	coef	std err	z	P>|z|
Intercept	0.8835	0.046	19.294	0.000
z_age	-0.0205	0.048	-0.425	0.671
z_tau	-0.0205	0.046	-0.447	0.655
z_pr	0.1187	0.048	2.466	0.014

Fig. 6. Direct Investigation into the Physiological Properties of Neural Maturation

(A) Reservoir network built from a Purkinje-cell conductance model. Two hundred neurons (50% excitatory, 50% inhibitory) were recurrently connected with random synaptic delays; background Poisson input sustained intrinsic activity. A 1,200-step Mackey–Glass series was used; the first 800 steps trained the readout on-line (delta rule), followed by a 100-step washout and a 300-step prediction phase. Plots show mean ± SEM across 30 seeds. Bottom panels: maximal Lyapunov exponent estimated from the first two principal components of reservoir states while driven by the Mackey–Glass input; memory capacity (MC) computed after washout from 500 + 20 recorded states using ridge-regression reconstructions at delays 1–20 with stratified five-fold shuffle cross-validation (MC = mean R^2 across valid delay × fold). Right-hand column repeats the analysis for the KCNH7-mutant channel (Fig. 4). (B) Continuous Mackey–Glass learning trajectories for Phase-A and Phase-B across KCNH7 conductance scales (WT and MUT), with magnified early-phase panels. Right-hand plots relate initial catch-up magnitude to the maximal Lyapunov exponent for each genotype/scale. (C) Cumulative MSE (mean ± SEM; N = 30). “WT only,” “MUT only,” and “GPCR-pulse” conditions manipulate the KCNH7 activation shift (vshift) as follows: WT only = +0 mV throughout; MUT only = +10 mV throughout; GPCR-pulse = +0 mV baseline with transient +10 mV pulses during gray windows (Phase-A: steps 100–129, 500–529, 950–979; Phase-B: steps 1250–1279, 1500–1529; 30 steps each). Vertical dashed lines indicate train, washout, test, and adapt boundaries. (D) Visual Behavior two-photon (VB2P) data. OPHYS 1–6 sessions with ≥ 10 cells and ≥ 10 trials were included (1,063 sessions; 101 mice). Variables were z-scored within mouse; multivariate relationships were assessed with Huber-robust regression.